COMPOSITES OF POLYVINYL ALCOHOL AND CHITOSAN REINFORCED WITH ZINC OXIDE NANOPARTICLES FOR REGENERATIVE THERAPY

COMPÓSITOS DE ALCOHOL POLIVINÍLICO Y QUITOSANO REFORZADOS CON NANOPARTÍCULAS DE ÓXIDO DE ZINC PARA TERAPIA REGENERATIVA

Carlos David Grande-Tovar[(1)] *, Lemy Vanessa Barba-Rosado[(2)], Carlos Humberto Valencia-Llano[(3)]

[1] *PhD, Chemist, Research Professor, Universidad del Atlántico, Grupo de Investigación de Fotoquímica y Fotobiología, Puerto Colombia- Colombia. [2]Chemist, Universidad del Atlántico, Grupo de Investigación de Fotoquímica y Fotobiología. [3]PhD, Research Professor, Universidad del Valle, Grupo Biomateriales Dentales, Escuela de Odontología, Cali-Colombia.

*Correspondence carlosgrande@mail.uniatlantico.edu.co.

Cite this article as: C. D. Grande-Tovar *, L. Barba-Rosado, C.H. Valencia-Llano "*Composites Of Polyvinyl Alcohol And Chitosan Reinforced With Zinc Oxide Nanoparticles For Regenerative Therapy*", Prospectiva, Vol. 23 N° 1 2025.

Recibido: 4/06/2024 / Aceptado: 20/11/2024
http://doi.org/ 10.15665/rp.v23i1.3565

ABSTRACT

Recently, the demand for alternative therapies for tissue restoration based on biomaterials that facilitate tissue restoration processes and avoid microbial infections has increased. In this work, we have synthesized four composite formulations based on polyvinyl alcohol (PVA), chitosan (CS), and zinc oxide nanoparticles (ZnO-NPs). The leading bands in the infrared spectrum of PVA and CS were evident, as well as the incorporation of NPs-ZnO. Thermogravimetric analysis (TGA) and differential scanning calorimetry (DSC) demonstrated that the interaction of the ZnO-NPs with the carbonyl group thermally destabilizes the composites. The morphological study using scanning

electron microscopy (SEM) showed that the composites incorporated with ZnO-NPs present an irregular and rough porous microstructure due to the evaporation of the solvent. Examination of the implanted composites by histological analysis demonstrated their biocompatibility and biodegradability 60 days after implantation. The simultaneous degradation and formation of type I collagen fibers, with increased blood vessels and inflammation, indicate a highly biocompatible and resorbable material, which could potentially revolutionize regenerative therapy.

Keywords: Compósitos de quitosano; Alcohol polivinílico; Ingeniería de tejidos; Nanopartículas de óxido de zinc.

RESUMEN

Recientemente, ha aumentado la demanda por terapias alternativas para la restauración de tejidos basadas en biomateriales que faciliten los procesos de restauración del tejido y eviten infecciones microbianas. En este trabajo, se sintetizaron cuatro formulaciones de composites basados en alcohol polivinílico (PVA), quitosano (CS) y nanopartículas de óxido de zinc (ZnO-NPs). Las principales bandas en el espectro infrarrojo del PVA y del CS fueron evidenciadas, así como la incorporación de las NPs-ZnO. El análisis termogravimétrico (TGA) y la calorimetría de barrido diferencial (DSC) demostraron que la interacción de las ZnO-NPs con el grupo carbonilo desestabiliza térmicamente a los composites. El estudio morfológico mediante microscopía electrónica de barrido (SEM) demostró que los composites incorporados con ZnO-NPs presentan una microestructura porosa irregular y rugosa, debido a la evaporación del solvente. El examen de los composites implantados mediante análisis histológico demostró su biocompatibilidad y biodegradabilidad 60 días después de la implantación. La degradación simultánea y la formación de fibras de colágeno de tipo I, con el aumento de los vasos sanguíneos y la inflamación, indican un material altamente biocompatible y reabsorbible, lo que podría potencialmente revolucionar la terapia regenerativa.

Palabras clave: Chitosan composites; Polyvinyl alcohol; Tissue engineering; Zinc oxide nanoparticles.

1. INTRODUCTION

Tissue regenerative therapy uses biological materials to repair damaged tissues, providing promising solutions for injuries, diseases, and defects [1]. However, the constant need for devices that can induce tissue restoration without rejection or inadequate immune responses has led researchers to explore new ways to achieve tissue restoration. One emerging new therapy is tissue regeneration using scaffolds made from a combination of biodegradable synthetic and natural polymers [2]. These scaffolds improve cell adhesion and provide an ideal setting for regeneration [3].

Among the synthetic biodegradable polymers used for tissue regenerative therapy is polyvinyl alcohol (PVA), a synthetic polymer with tremendous potential for tissue regeneration, which is regularly used due to its biocompatibility, ability to tailor its mechanical properties, and high hydrophilicity, making it a versatile material [4]. PVA can be applied in various forms, such as hydrogels and scaffolds, and mixed with other polymers, such as chitosan, gelatin, and silk-fibroin, to promote cell growth and facilitate tissue regeneration [5–9]Nonetheless, further research is required to optimize its properties and examine its potential in regenerative medicine when mixed with other biopolymers or nanomaterials.

Likewise, chitosan, a biopolymer derived from chitin present in fungi and crustaceans, boasts an array of beneficial properties. Among them are biodegradability, biocompatibility, and antimicrobial activity [10–12]. When acted upon by enzymes, chitosan can be broken down and replaced by regenerated tissue. In regenerative therapy, chitosan is used for different purposes, such as drug delivery, wound healing, and tissue regeneration [13]Although research is underway to explore its full potential, thorough evaluations are essential to ensure its safety and efficacy in clinical settings.

Among the most promising nanomaterials for tissue engineering are zinc oxide nanoparticles (ZnO-NPs), a highly stable and cost-effective semiconductor that the FDA has approved for safe use [14]. They can be synthesized through various techniques, including precipitation, sol-gel, spray pyrolysis, thermal decomposition, and forced solvolysis [15]. ZnO-NPs possess antimicrobial properties and are utilized in multiple applications, including textiles, packaging, and medicine [16]. Nanocomposites incorporating ZnO-NPs have demonstrated impressive effectiveness in fighting bacteria and improving biocompatibility.

Gutha et al. studied the antimicrobial and wound-healing capacity of CS/PVA beads and ZnO nanoparticles. The antibacterial activity (evaluated on *Escherichia coli* and *Staphylococcus aureus*) was higher in the CS/PVA/ZnO mixture compared to the CS/PVA polymeric matrix. The wound healing activity, evaluated on mouse skin, confirmed that the CS/PVA/ZnO dressing promotes wound healing; furthermore, histological studies showed the formation of the dermis and epidermis, demonstrating accelerating wound healing and control of bacterial growth [17].

Sirotkin et al. studied a composite for wound healing in mice based on PVA and chitosan by incorporating nanoparticles or metal oxides (Ag NPs, ZnO NPs, Cu NPs). Patch coating of chitosan/PVA composite with ZnO NPs positively affected wound healing and complete wound closure. Histological examination showed cell proliferation at 9 and 10 days, demonstrating the antioxidant and antibacterial capabilities of zinc oxide and a synergistic effect between polymers and ZnO NPs [18].

The integration of PVA/CS/ZnO-NPs into composites may revolutionize tissue regeneration therapy. Previous research has already demonstrated the potential of the PVA/CS polymer matrix.

[19–23], but have not been studied with ZnO-NPs through the drop-casting methodology (Figure 1). This study aims to demonstrate that composites of PVA/CS/ZnO-NPs improve subdermal tissue in male Wistar rats and accelerate cell adhesion and wound closure without the formation of a fibrous capsule. We believe that the results of this investigation present a significant opportunity for advancements in the fields of tissue engineering and therapeutic medicine.

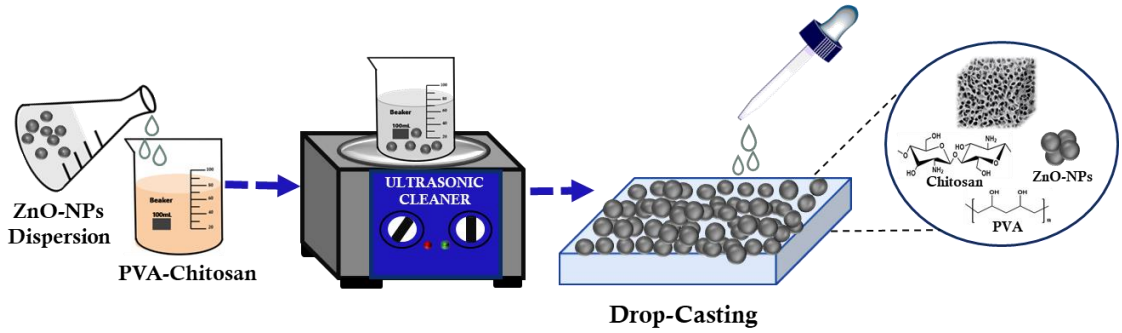

Figure 1. Drop-casting methodology for the fabrication of PVA/CS/ZnO-NPs composites.

2. Materials and Methods

2.1. Materials

The reagents used in this investigation were not purified. Chitosan had a low molecular weight (1 × 10^6 Da), over 80% deacetylation, and a 20–300 cP viscosity. Polyvinyl alcohol had 90% hydrolysis and 95,000 g/mol. ZnO-NPs were synthesized from Merck using ZnCl2 (80%), 99% NaOH, and 99.8% 2-propanol.

2.2. Synthesis of ZnO-NPs

ZnO-NPs were synthesized by mixing 0.2M $ZnCl_2$ and 5M NaOH solution and stirring at 90°C [24]. The residue was washed with water and ethanol to remove NaCl. Purification was done using centrifugation and washing with 2-propanol in triplicate. The ZnO-NPs were calcined at 250°C for five hours.

2.3. Preparation of the PVA/CS/ZnO-NPs composites

We synthesized PVA/CS/ZnO-NPs composites using a drop-casting technique with 4% total solids content, as previously reported [21]. ZnO-NPs were ultrasonicated in water at 300 mg/ml for 2 hours. Components were dissolved in 1% acetic acid and mixed according to Table 1. The mixture was degassed in an ultrasonic bath, poured onto glass molds, and then baked at 40°C ± 0.2 to obtain PVA/CS/ZnO-NPs membranes.

Tabla 1. Formulación de las membranas de PVA/CS/ZnO-NPs

Table 1. Formulation of PVA/CS/ZnO-NPs composites.

Components	PVA (%)	CS (%)	ZnO-NPs (%)
F1	70	30	0
F2	70	29.5	0.5
F3	70	29.0	1.0
F4	70	28.0	2.0

2.4. Characterization of the ZnO-NPs

The synthesis and characterization of ZnO-NPs was followed according to previous reports[24].

2.5. Characterization of PVA/CS/ZnO-NPs composites

2.5.1 X-ray diffraction (XRD) and Fourier transform infrared spectroscopy (FTIR).

XRD analysis was performed using a PANalytical X0Pert PRO diffractometer (Malvern Panalytical, Jarman Way, Royston, UK) with a Cu anode at a wavelength of Kα1 (1.540598 Å). Diffractograms were taken in the 5-80° range with a scan speed of 2.63 s, scan rate of 2 degrees/min, and a step size of 0.01°. Attenuated Total Reflectance-Fourier Transform Infrared Spectroscopy (ATR-FTIR) acquired information about functional groups and molecular interactions in the 500-4000 cm^{-1} range using an FT-IR-8400 instrument (Shimadzu, Kyoto, Japan) with a spectral resolution of 4 cm^{-1} and 32 scans.

2.5.2 Thermal Analysis of the PVA/CS/ZnO-NPs composites

The thermogravimetric analysis (TGA) was performed using a NETZSCH TG 209 F1 Libra instrument from Mettler Toledo (Schwerzenbach, Switzerland). The samples were heated from 25-800°C at a rate of 10°C/min under nitrogen, using an Al_2O_3 crucible.

Thermodynamic properties were obtained using differential scanning calorimetry (DSC) with a DSC1/500 instrument (Mettler Toledo, Schwerzenbach, Switzer-land) in a nitrogen atmosphere. The first heating was performed from 0°C to 250°C with a ramp of 10°C/min and nitrogen flow of 60 mL/min. There, it was maintained at 250°C for 2 minutes. Then, the cooling was performed from 250°C to 0°C with a ramp of -10°C/min and nitrogen flow of 60 mL/min, where it was kept at 0°C for 2 minutes. Then, the second heating was performed from 0°C to 350°C with a ramp of 10°C/min and nitrogen flow of 60 mL/min. In this way, properties such as glass transition temperature (T_g) calculated with the midpoint of the transition and melting temperature (Tm) were obtained from the endothermic peaks. Finally, the crystallization temperature (Tc) was calculated from the exothermic peak. TA Instruments' Universal Analysis Software 2000 version 4.5A was utilized to determine the properties above.

2.5.3 Scanning Electron Microscopy Analysis

The PVA/CS/ZnO-NPs composite morphologies were collected using a JEOL JSM-6490LA equipment (Musashino, Tokyo, Japan) in the secondary electron mode at 20 kV. The samples were coated with a gold layer.

2.6 Surgical preparation of biomodels

PVA/CS/ZnO-NPs composites were implanted in the subdermal tissue of three adult male Wistar rats, six months old and weighing an average of 380 grams. The number of animals, sites to be implanted, and sample size were determined according to ISO 10993-6 [25]. The biomodels were supplied by the LABBIO laboratory of the Universidad del Valle, Cali, Colombia. They remained under their care during the 90 days of implantation with food and water available at will.

The authorization and ethical supervision were carried out by the animal ethics committee CEAS of the Universidad del Valle, Cali, Colombia, using the "ACTA DE AVAL A PROYECTOS DEL ÁREA BIOMEDICA N° (006) AÑO (2022)". The recommendations of the "Animal Research: Reporting of In Vivo Experiments" (The ARRIVE guidelines) were also taken into account [26]. This study took into account the three Rs principle of Rusell and Burch, especially the replacement principle when determining the number of animals by ISO 10993-6 [25], and refinement by using protocols already established in the scientific literature.

During the animal surgeries, a sedative was administered consisting of a combination of Ketamine (Blaskov Laboratory, Bogota, Colombia) and Xylazine (ERMA Laboratories, Celta, Colombia) in a 70/30 ratio. Once the sedative took effect, the dorsal surface of the right side of the skin was shaved and disinfected using an Isodine solution (Laboratory Sanfer, Bogota, Colombia). The area to be operated on was then anesthetized with Lidocaine 2% with Epinephrine 1:80000 (New Stetic, Guarne, Antioquia) using an infiltrative technique. To prepare for the operation, four 5-millimeter incisions were made, and four pockets measuring 20 mm in depth and 5 mm in width were created in each animal using a blunt cylindrical instrument with a diameter of 5 millimeters.

Once the pockets were ready, we inserted small 10mm × 15mm sheets and closed them using a basic stitch technique utilizing four zeros resorbable sutures. Topical gentamicin was applied to the wounds, and intramuscular diclofenac 75mg was administered (Genfar Laboratory Bogotá, Colombia). Control material was not used as these products are typically biocompatible and bioresorbable, providing no additional information beyond the normal healing process during sample recovery and minimizing the number of affected areas. During the time the experiment lasted, there were no intraoperative or postoperative complications nor deaths of biomodels; after three months, the sacrifice was performed using a euthanasic drug in the intraperitoneal application (Euthanex, INVE Laboratory, Cota, Colombia).

The samples were recovered and fixed for 48 hours in buffered formalin. Then, they were washed with buffer solution, and the histological preparation of the samples was performed. The preparation of the samples consisted of dehydration with alcohols, clarification with xylol, and inclusion with kerosene using the Leca TP 120 (Leica Microsystems, Mannheim, Germany).

2.6.1 Histological Analysis

Subsequently, paraffin blocks were created with the tissue included using the Thermo Scientific™ Histoplast Paraffin™ kit (Fisher Scientific, Waltham, Massachusetts, USA), and 6-micrometer slices were made using a Leica RM2135 microtome.

For visualization of histological structures, staining was performed with Hematoxylin-Eosin (HE), Gomori trichrome (GT), and Masson trichrome (MT) techniques using standardized protocols. Images were analyzed using a Leica DM750 optical microscope with a built-in Leica DFC 295 camera and Leica Application Suite version 4.12.0 software (Leica Microsystem, Mannheim, Germany).

3. Results and Discussion

3.1. Characterization of ZnO-NPs

Zinc oxide nanoparticles (ZnO-NPs) were produced and analyzed using established procedures [24].

3.2. FT-IR Spectroscopy

Figure 2 illustrates the analysis of the different functional groups found in the composites. For example, the C-O bond stretching vibrations in CS and PVA contribute to the bands appearing in the 900-1100 cm^{-1} range [27]. The peak observed at 1560 cm^{-1} is attributed to the NH bending (amide II), while the small peak at 1650 cm^{-1} is assigned to C=O stretching (amide I) [28]. The bands observed at 1250, 1320, and 1410 cm^{-1} are associated with the pyranose ring [28]. Symmetric tension bands at 3331 cm^{-1} were observed, related to the -OH groups in PVA and CS and the intermolecular hydrogen bonds between O-H groups of both polymers [29,30]. This O-H band could overlap with the N-H stretching peaks of amines [31]. Likewise, the symmetric and asymmetric tension band of the alkyl groups CH and CH_2 at 2939 cm^{-1} was observed. In addition, the tension band of the carbonyl group (C=O) at 1726 cm^{-1} was related to the stretching of the C=O from the acetate group of PVA that was not wholly hydrolyzed [32,33]Finally, the symmetric tension band of the aliphatic C-O-C ester group at 1035 cm^{-1}. Likewise, the corresponding -C-O stretching vibrations occur at 1085 cm^{-1}, belonging to the polymer blend. On the other hand, adding ZnO-NPs to CS and PVA bonds (F3 and F4) did not alter the spectra, indicating a homogeneous dispersion within the polymeric matrix.

Figura 2. Espectro FT-IR de los compósitos de PVA/CS/ZnO-NPs. F1, 70%PVA/30%CS; F2, 70%PVA/29.5%CS/0.5%ZnO-NPs; F3, 70%PVA/29.0%CS/1.0%ZnO-NPs; F4, 70%PVA/28.0%CS/2.0%ZnO-NPs.

Figure 2. FT-IR spectrum of PVA/CS/ZnO-NPs composites. F1, 70%PVA/30%CS; F2, 70%PVA/29.5%CS/0.5%ZnO-NPs; F3, 70%PVA/29.0%CS/1.0%ZnO-NPs; F4, 70%PVA/28.0%CS/2.0%ZnO-NPs.

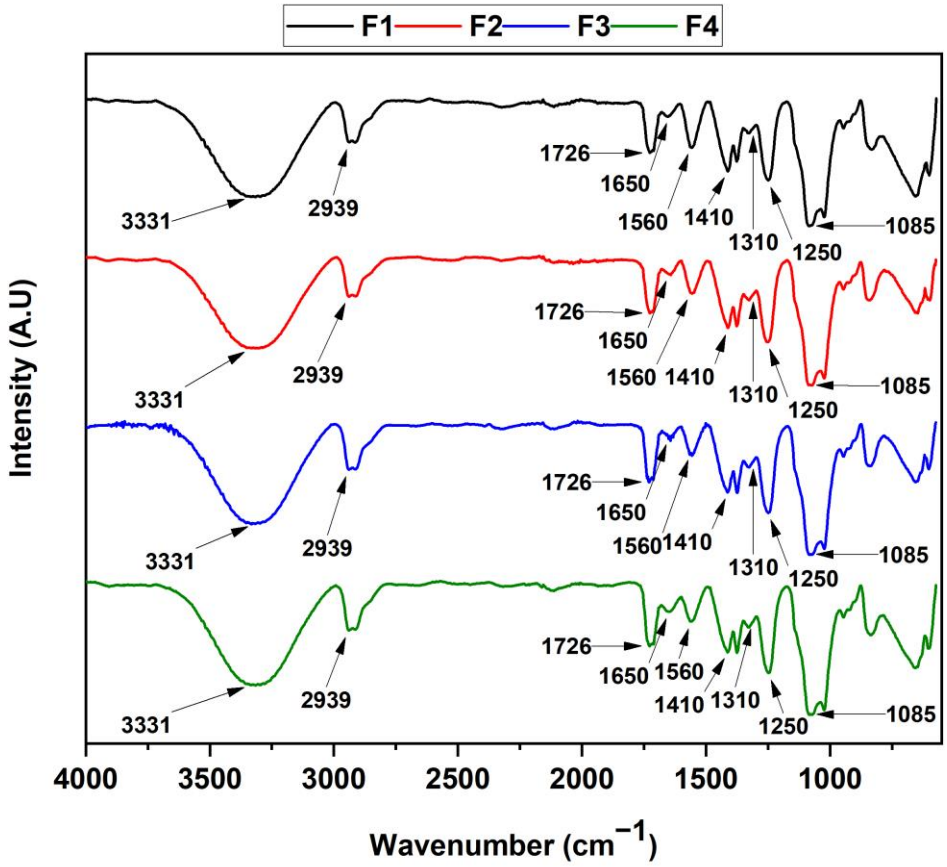

3.4. X-ray Diffraction

X-ray diffraction analysis provides information on the composites' amorphous and crystalline physical forms. Figure 3 shows characteristic peaks of the CS/PVA polymer matrix: a low-intensity peak at 2θ=11.3°, a prominent peak at 2θ= 19.3°, and two intense peaks at 2θ=16.6° and 22.2° [31,34]. The latter peak is evidence of the semi-crystalline nature of the CS/PVA polymer blend, which could be attributed to intermolecular and intramolecular interactions through hydrogen bridges between the polymer chains [35,36].

On the other hand, it was observed that by reducing the concentration of chitosan in formulations F2, F3, and F4, there was a decrease in the intensity of the peak at 2θ=19.3°. Formulation F2 was the one that presented the most significant decrease. In F3, the reduction was less pronounced. This decrease suggests a disorder in the chitosan chains, retaining the crystalline phase of the polymer. This change in intensity could be due to the breaking of intermolecular hydrogen bonds by inserting the PVA chains between the chitosan chains [37].

For formulation F4, no decrease in the intensity of the 2θ=19.3° peak was observed; however, increasing the concentration of ZnO-NPs to 2% may have increased the crystallinity of the composite by generating possible electrostatic interactions and hydrogen bonds with the polymer matrix. Additionally, an increase in ZnO-NPs content (2%) in F4 leads to an increased peak at 2θ=16.6°, indicating a rise in crystallinity [38].

Figura 3. Análisis DRX de las membranas PVA/CS/ZnO-NPs.

Figure 3. XRD analysis of PVA/CS/ZnO-NPs composites.

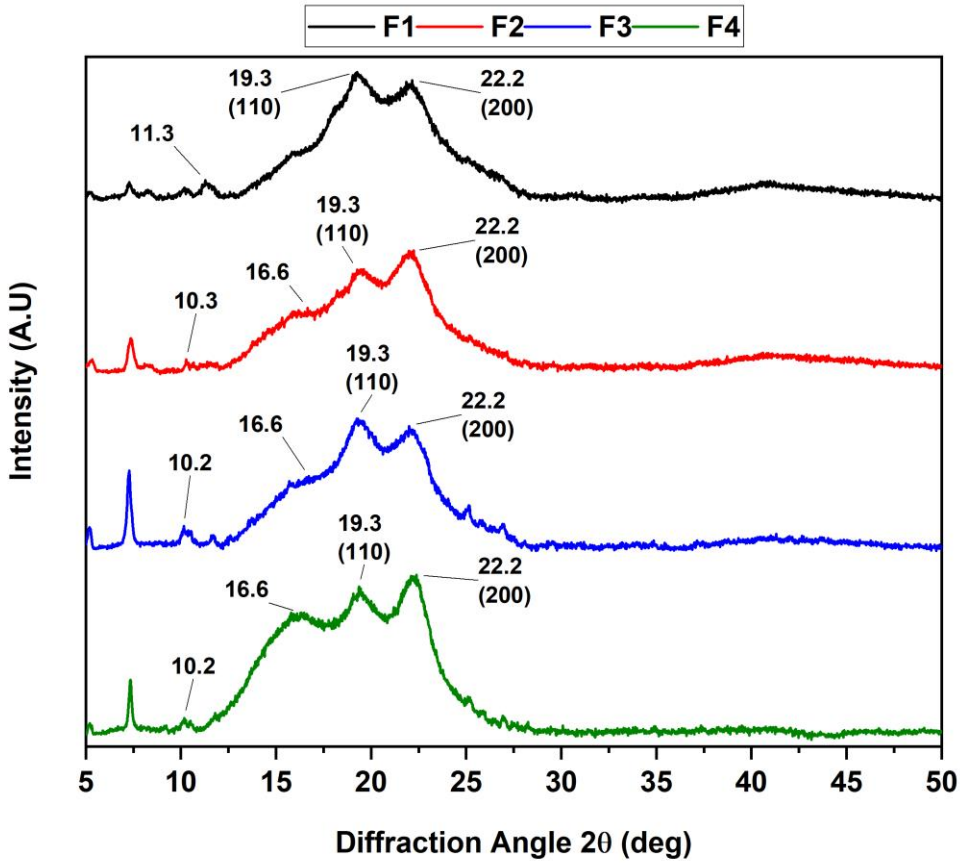

3.5. Thermal Analysis of PVA/CS/ZnO-NPs composites.

TGA allows the analyst to provide information about the formulation performed to the material's thermal properties. For this purpose, the thermal degradation by weight caused by increasing temperature is evaluated. Figure 4A shows PVA/CS/ZnO composite thermograms, and Figure 4B their derivatives. The formulations exhibit three degradation stages but with apparent differences. The first degradation stage between 50-100°C is attributed to water evaporation physically adsorbed. For F1, there is a higher loss of approximately 17% at lower temperatures than the other

three formulations, with F3 as the most stable formulation. The second degradation stage is between 200-300°C, attributed to the PVA side chain degradation, with a maximum temperature degradation of around 297 °C for F1, F2, and F3, but F4 decreased the maximum temperature to 253°C. Finally, the third degradation is between 300-500°C, with the maximum degradation temperature AT 477°C (Figure 4B) corresponding to the degradation of the glycosidic linkages of the CS and the degradation of residual polyenes from PVA. Adding ZnO-NPs introduces thermal stability, especially for F3, which increases the temperature for the mass loss for the second and third degradation stages by approximately 5% and 17%, respectively, compared to F1. This stability is possible due to the interaction of the hydrogen bonds of the PVA/CS polymeric matrix and the oxygen bonds of the O-Zn-O [39,40]. When ZnO-NPs are homogeneously dispersed, they create a barrier against degradative gases and improve the mechanical behavior of the composite because the polymeric components interfere with heat transfer and better support the charge transfer [41,42]. Studies have found that ZnO acts as a thermal insulator that restricts the movement of polymer chains and decreases the permeability of volatile products through the material [43,44].

Figura 4. Análisis termogravimétrico de los compositos de PVA/CS/ZnO-NPs F1, F2, F3 y F4.

Figure 4. Thermogravimetric analysis of the PVA/CS/ZnO-NPs composites F1, F2, F3, and F4.

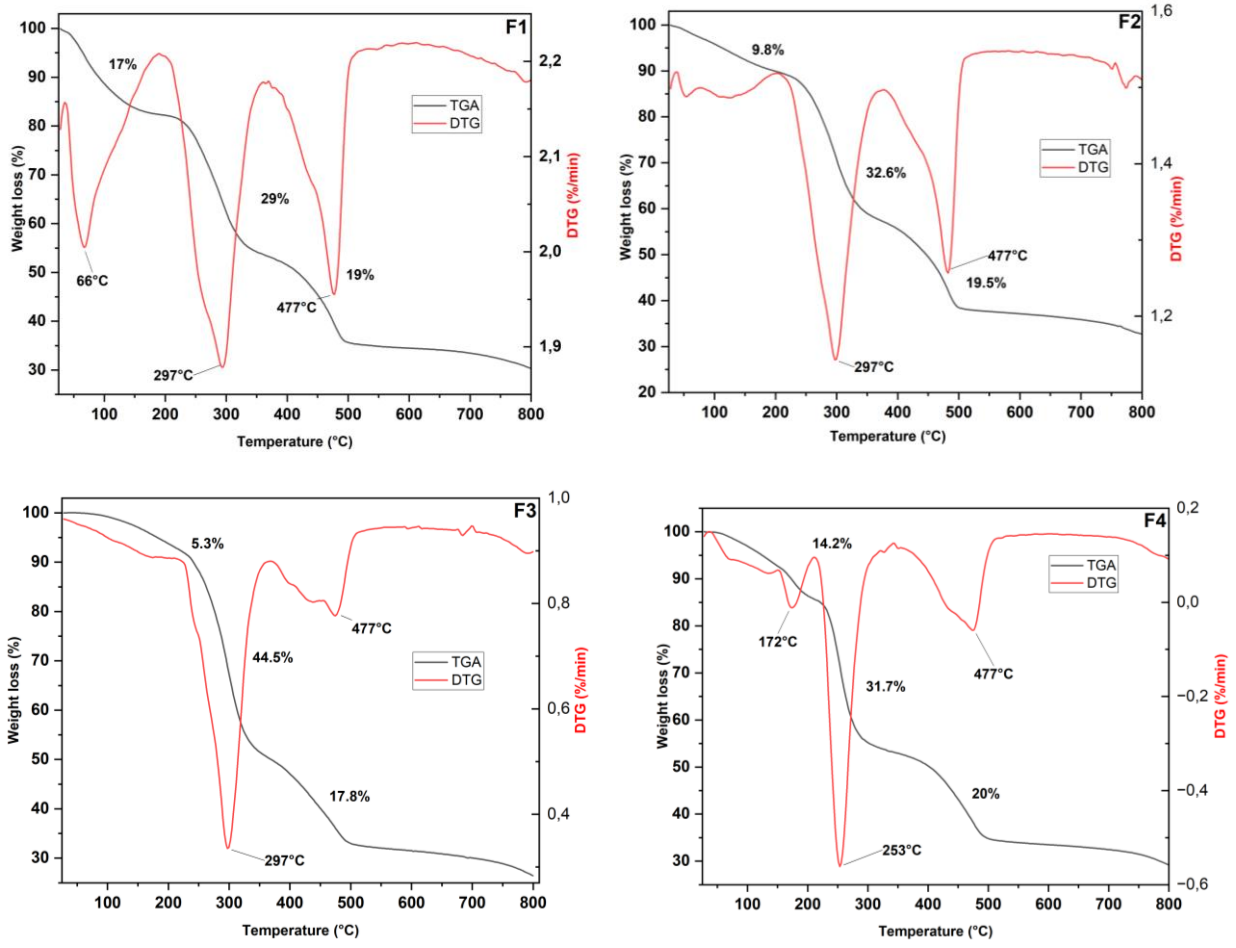

The different thermograms obtained by differential scanning calorimetry (DSC) were analyzed to evaluate the thermal stability of the PVC/CS polymer matrix and ZnO composites in each formulation. Endothermic peaks with temperature shifts were found. The first endothermic peak, recorded between 70 °C and 90° C in each formulation, is attributed to the initial loss of adsorbed water from each formulation, reflecting differences in the water holding capacity of each formulation, with the decrease in formulation F4 being notable.

Different studies have reported that the melting temperature of PVA is approximately 230 °C; however, in the blending of the polymers, changes in temperature may occur [36,45]The endothermic peak corresponding to the melting temperature was found between 150 °C and 165 °C, with formulations F3 and F4 showing the most significant decreases. This could be due to the increase in NPs-ZnO in these formulations, which generates possible interactions between NPs-ZnO and the polymeric matrix. Regarding the endothermic peaks between 290 °C and 320 °C, related to polymer degradation, formulations F3 and F4 showed a decrease at temperatures 297 °C and 293 °C, respectively.

Figura 5. Curvas DSC de los composites de PVA/CS/ZnO-NPs.

Figure 5. DSC curves of the PVA/CS/ZnO-NPs composites.

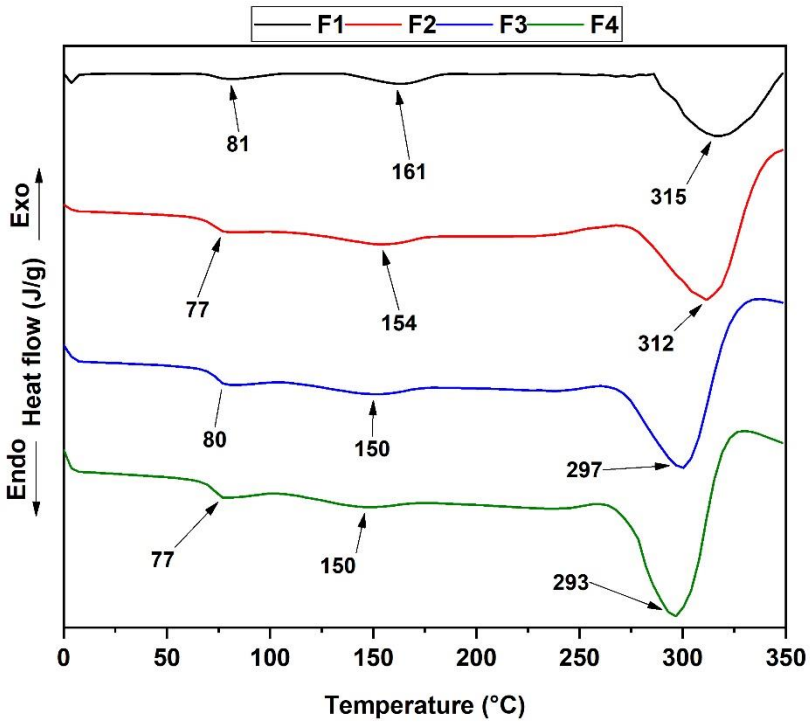

3.6 Scanning Electron Microscopy (SEM) of PVA/CS/ZnO-NPs composites.

Figure 6 depicts the morphological microstructure of the PVA/CS/ZnO-NPs composites. All the composites exhibit a notable roughness and porosity conducive to cell adhesion and proliferation. Notably, an increase in the amount of ZnO-NPs results in a more homogeneous surface, indicating successful dispersion of the nanoparticles within the polymer chains. Additionally, incorporating ZnO-NPs leads to a smoother surface, whereas phase separation between the polymers with small microdomains is observed in F1-F3. These observations indicate the potential utility of PVA/CS/ZnO-NPs composites for biomedical applications.

Figura 6. Morfología de los composites de PVA/CS/ZnO-NPs. F1, 70%PVA/30%CS a 200×; F2, F2, 70%PVA/29.5%CS/0.5%ZnO-NPs a 200×; F3, 70%PVA/29.0%CS/1.0%ZnO-NPs a 200×; F4, 70%PVA/28.0%CS/2.0%ZnO-NPs a 200×.

Figure 6. Morphology of PVA/CS/ZnO-NPs composites. F1, 70%PVA/30%CS at 200×; F2, F2, 70%PVA/29.5%CS/0.5%ZnO-NPs at 200×; F3, 70%PVA/29.0%CS/1.0%ZnO-NPs at 200×; F4, 70%PVA/28.0%CS/2.0%ZnO-NPs at 200×.

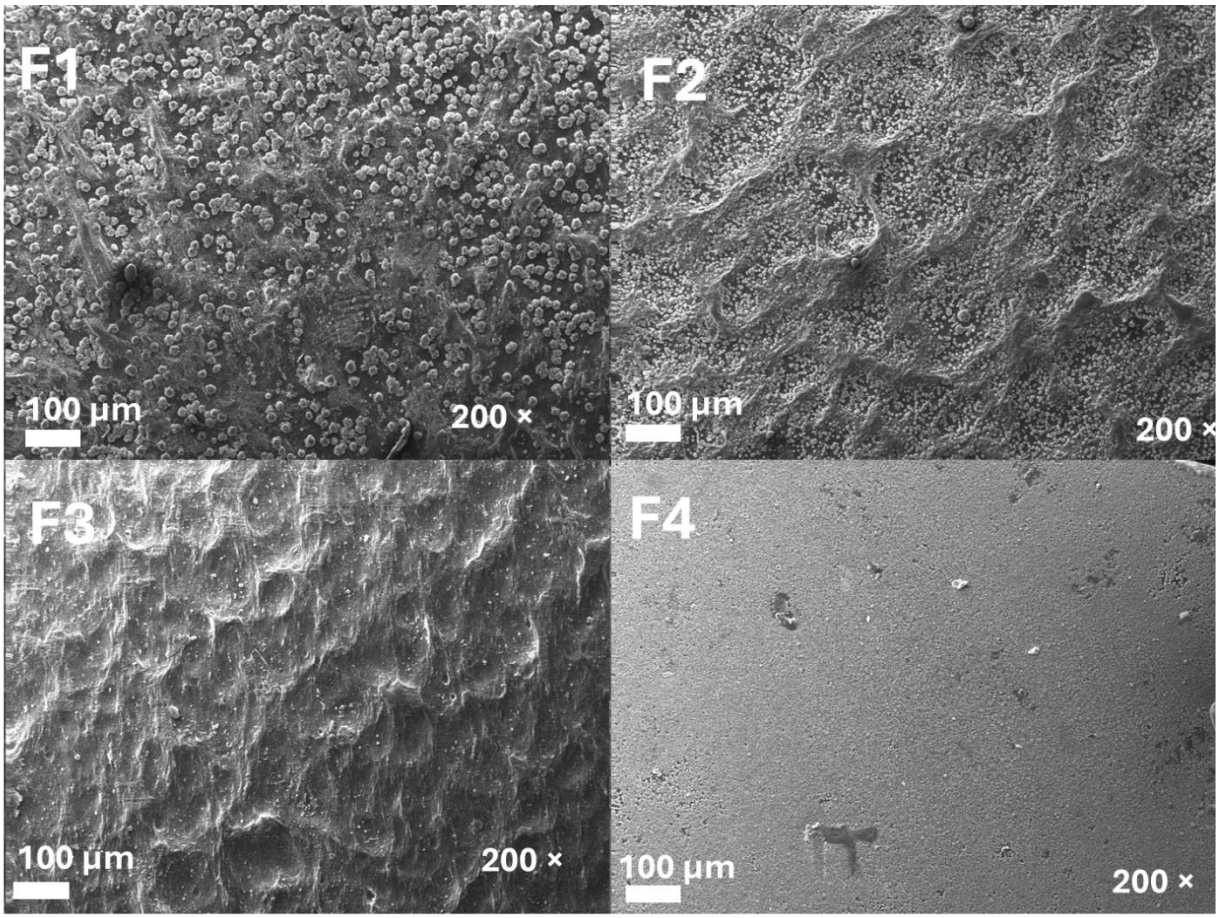

3.7. In Vivo Biocompatibility Tests of the PVA/CS/ZnO-NPs composites

Once euthanasia was performed, a macroscopic inspection of the implanted areas was performed; Figure 7 corresponds to the macroscopic view of the intervened areas. In Figure 7A, after 90 days, complete hair growth is observed in the dorsal area. In Figure 7B, after shaving, the area is completely healed. In Figure 7C, corresponding to the subcutaneous surface in positions F1, F2, and F3, the areas where the materials were implanted with a slight induration and color change can be appreciated; in position F4, there is no induration or color change, the tissue that is observed corresponds to an adhesion of tissue that remained when separating the skin, the tissue that is observed corresponds to an adhesion of tissue that was left when separating the skin.

The macroscopic images of the four intervened areas indicate a normal healing process in which hair recovers, complete removal of the sutures, complete healing of the skin, and the absence of fistulas and necrotic tissue on the internal surface occurs. Histological studies made it possible to visualize how healing happened in the intervened areas in the presence of the four formulation types.

Figura 6. Aspecto macroscópico de las zonas implantadas. A: Recuperación de vello. B: Superficie después de realzar tricotomía. C: superficie interna de la piel. F1: Zona implantación formulación 1. F2: Zona de implantación formulación 2. F3: Zona de implantación formulación 3 y F4: Zona de implantación formulación 4.

Figure 6. Macroscopic aspect of the implanted areas. A: Hair regrowth. B: Surface after trichotomy enhancement. C: the inner surface of the skin. F1: Implantation zone formulation 1. F2: Implantation zone formulation 2. F3: Implantation zone formulation 3 and F4: Implantation zone formulation 4.

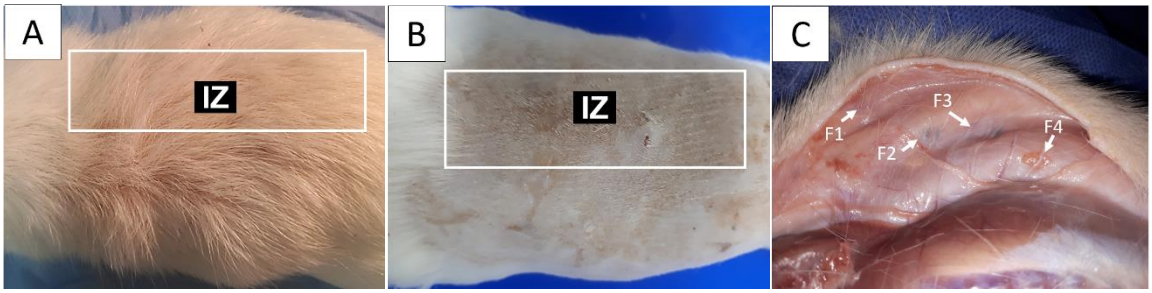

3.7.1 Biocompatibility of formulation F1 (PVA 70%/CS 30%)

Sample F1 corresponds to a film of the material composed of 30% CS and 70% PVA; Figure 8 corresponds to the microscopic images. At 90 days after implantation, the implanted material is observed in the process of fragmentation and with minor resorption (Figure 8A, 8B, and 8C); the material is surrounded by a fibrous capsule composed of type III collagen fibers, green in Figure 8B, evidenced by Gomori's trichrome technique, and by type I collagen fibers, blue in Figure 8C, evidenced by Masson's trichrome technique. The collagen fibers that form the capsule appear to

come from both the dermis and the muscular epimysium, as indicated by the purple arrows in Figure 8C.

A fibrous capsule surrounding the implanted material is a common and widely reported finding. It corresponds to a foreign body reaction in which, as inflammation persists, the body may attempt to isolate the biomaterial from the surrounding tissue by forming a fibrous capsule. Connective tissue cells (fibroblasts) deposit collagen around the biomaterial, forming an encapsulating structure. This capsule limits the interaction between the biomaterial and the surrounding tissues while the degradation/resorption process of the implanted material takes place [46–48].

Figura 8. Muestra F1 a 90 días de implantación. A: imagen a 4×; técnica HE; D: dermis; IZ: Zona de implantación; Óvalo negro: zona de implantación; M: Músculo; Fc: Cápsula fibrosa, Estrellas amarillas: Fragmentos del material implantado. B: Imagen a 4×; técnica GT; D: dermis; M: Músculo; Fc: Cápsula fibrosa, Estrellas amarillas: Fragmentos del material implantado. C: Imagen a 4×; técnica MT; D: dermis; M: Músculo; Fc: Cápsula fibrosa, Flechas moradas: Fibras de Colágeno tipo I. Estrellas amarillas: Fragmentos del material implantado.

Figure 8. F1 specimen 90 days after implantation. A: 4× image; HE technique; D: dermis; IZ: implantation zone; Black oval: implantation zone; M: muscle; Fc: fibrous capsule; Yellow stars: fragments of implanted material. B: 4× image; GT technique; D: dermis; M: muscle; Fc: fibrous capsule; Yellow stars: fragments of the implanted material. C: 4× image; MT technique; D: dermis; M: muscle; Fc: fibrous capsule, Purple arrows: Collagen type I fibers. Yellow stars: Fragments of the implanted material.

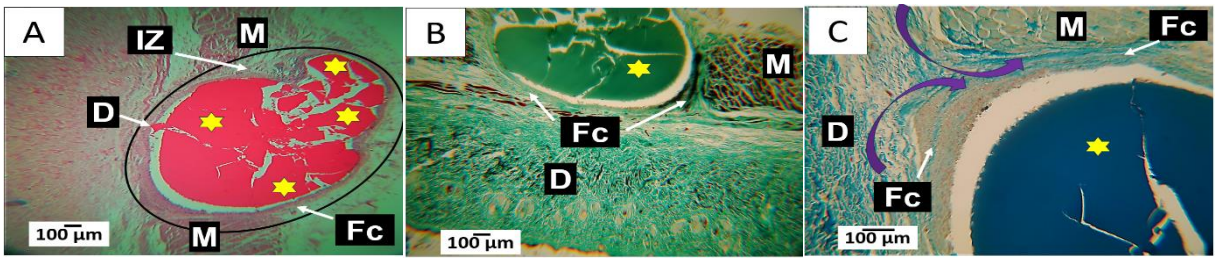

3.7.2 Biocompatibility of formulation F2 (PVA 70%/CS 29.5%/ZnO-NPs 0.5%)

Formulation F2 presents lower chitosan than F1, and 0.5% ZnO-NPs were incorporated. These changes were reflected histologically with an increase in the degradation/resorption of the material (Figure 9). Figure 9A shows the changes in the material degradation. The samples are fragmented and surrounded by an inflammatory infiltrate (Figure 9A). In the middle of the inflammatory infiltrate, with moderate coloration in the HE staining technique, tiny fragments of the material and areas where the material has disappeared through the phagocytic action of the inflammatory cells are observed. Figures 9B and 9C show the persistence of a fibrous capsule composed of type I and III collagen fibers, like those reported for the F1 formulation; these fibers appear to come from both the dermis and the epimysium (Figure 9C).

After 90 days of implantation, the foreign body reaction-type inflammatory response is still present due to the fragments of the implanted material. Even though a significant part of the material has undergone fragmentation, resorption, and degradation, the continued presence of these fragments can explain the presence of the fibrous capsule.

Chitosan (CS) and polyvinyl alcohol (PVA) are two materials that are both compatible with living tissues and can be naturally broken down by the body. While CS has excellent biological properties that make it an ideal material for creating scaffolds for tissue regeneration [49], its poor mechanical properties pose a challenge. To address this issue, researchers in this study combined CS with PVA. The F2 formulation also includes ZnO-NPs, which are biocompatible, biodegradable, and known to stimulate angiogenesis - the growth of new blood vessels [50].

It appears that the modifications implemented in the formulation have impacted the biological behavior of the implanted material. The heightened inflammatory response observed has accelerated the degradation of the material, which was also accompanied by a more significant cellular response, leading to faster reabsorption than the F1 formulation.

Figura 9. Muestra F2 a 90 días de implantación. A: imagen a 4×; técnica HE; IZ: Zona de implantación; Óvalo negro: zona de implantación; M: Músculo; Fc: Cápsula fibrosa, Estrellas amarillas: Fragmentos del material implantado; Estrellas rojas: infiltrado inflamatorio. B: imagen a 4×; técnica GT; D: dermis; M: Músculo; Fc: Cápsula fibrosa, Estrellas amarillas: Fragmentos del material implantado. C: imagen a 4×; técnica MT; D: dermis; M: Músculo; Fc: Cápsula fibrosa, Flechas moradas: Fibras de Colágeno tipo I. Estrellas amarillas: Fragmentos del material implantado.

Figure 9. F2 specimen at 90 days after implantation. A: 4× image; HE technique; IZ: implantation zone; black oval: implantation zone; M: muscle; Fc: fibrous capsule, yellow stars: fragments of implanted material; red stars: inflammatory infiltrate. B: 4× image; GT technique; D: dermis; M: muscle; Fc: fibrous capsule; Yellow stars: fragments of the implanted material. C: 4× image; MT technique; D: dermis; M: muscle; Fc: fibrous capsule. Purple arrows: Collagen type I fibers. Yellow stars: Fragments of the implanted material.

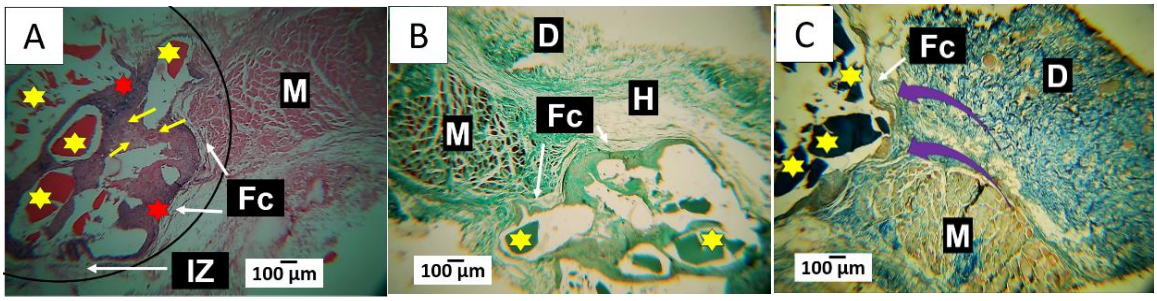

3.7.3 Biocompatibility of formulation F3 (PVA 70%/CS 29.0%/ZnO-NPs 1.0%)

The histological image of this formulation shows a more advanced degradation/resorption process than the other two formulations (see Figure 10A). A fibrous capsule still surrounds the implantation zone of collagen fibers (see Figure 10B), which appears to be of lesser thickness than the capsules observed for the implantation of the other two formulations.

Observations have shown that in regions with larger particles, these particles are typically surrounded by an inflammatory infiltrate that aids in their breakdown and absorption (Figure 10C). As the larger particles are broken down, smaller particles remain and are eliminated through phagocytosis by multinucleated cells. Consistent with previous findings, alterations in the percentages of particles appear to influence the degree of material fragmentation and its subsequent degradation and reabsorption by inflammatory cells. Notably, the participation of multinucleated cells in this process is emphasized as they play a crucial role in phagocytosing the final fragments of the material.

Figura 10. Muestra F3 a 90 días de implantación. A: imagen a 4×; técnica HE; D: dermis; IZ: Zona de implantación; Óvalo negro: zona de implantación; Fc: Cápsula fibrosa, Estrellas amarillas: Fragmentos del material implantado. B: imagen a 4×; técnica MT; D: Dermis; M: Musculo; Fc: Capsula fibrosa. C: Imagen a 4×; técnica HE; Estrellas amarillas: Fragmentos del material implantado. Ovalo blanco zona de reabsorción de un fragmento de material; Óvalos amarillos: Zonas de reabsorción de fragmentos muy pequeños con presencia de células multinucleares.

Figure 10. F3 specimen at 90 days after implantation. A: 4× image; HE technique; D: dermis; IZ: implantation zone; black oval: implantation zone; Fc: fibrous capsule, yellow stars: fragments of implanted material. B: 4× image; MT technique; D: Dermis; M: muscle; Fc: fibrous capsule. C: 4× image; HE technique; Yellow stars: Fragments of the implanted material. White oval: resorption zone of a fragment of material; Yellow ovals: resorption zones of tiny fragments with multinuclear cells.

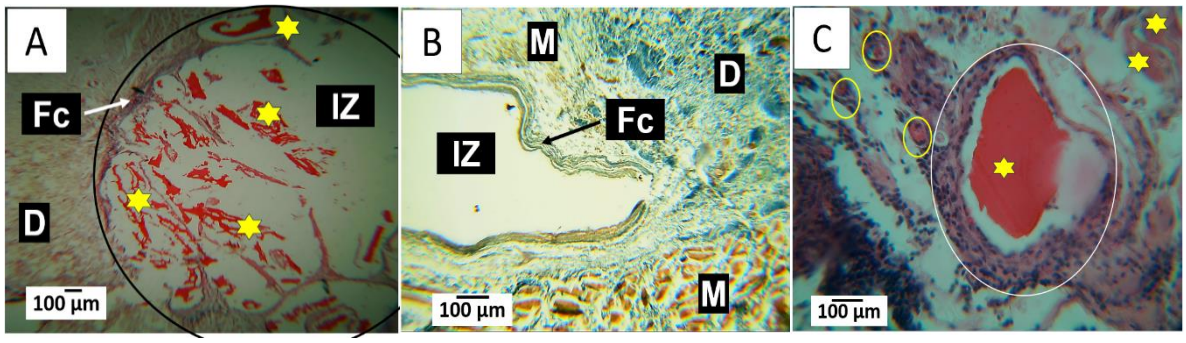

3.7.4 Biocompatibility of formulation F4 (PVA 70%/CS 28.0%/ZnO-NPs 2.0%)

The F4 formulation displays notable changes in the behavior of its components. After subdermal implantation for 90 days, histological images reveal near-complete degradation or resorption of the material (see Figure 11A). Additionally, there is a marked reduction in capsule thickness, as depicted in Figure 11B. Masson's trichrome staining was utilized to show remnants of the fibrous capsule, including some type I collagen fibers. The implantation zone's material space is gradually

replaced by connective tissue involving type III collagen, as evidenced by Gomori trichrome staining (Figure 11C). This figure also shows fragments of the F4 film in the middle of a connective tissue matrix, with no signs of the inflammatory infiltrate observed in the F2 and F3 formulations.

Figura 11. Muestra F4 a 90 días de implantación. A: imagen a 4×, técnica HE; D: dermis, IZ: Zona de implantación. Óvalo negro: zona de implantación. Estrella amarilla: Fragmentos del material implantado. B: Imagen a 4×, técnica MT. D: Dermis; M: Músculo. Fc: Cápsula fibrosa. IZ: Zona de implantación. Estrella amarilla: Fragmento del material implantado. C: Imagen a 40×; técnica GT. Estrellas amarillas: Fragmentos del material implantado. Estrellas moradas: tejido conectivo con presencia de colágeno tipo III.

Figure 11. F4 specimen 90 days after implantation. A: 4× image, HE technique. D: dermis. IZ: implantation zone. Black oval: implantation zone. Yellow star: fragments of implanted material. B: 4× image. MT technique; D: Dermis; M: muscle; Fc: fibrous cap. IZ: Implantation zone; Yellow star: Fragment of the implanted material. C: 40× image, GT technique. Yellow stars: fragments of the implanted material. Purple stars: connective tissue with the presence of type III collagen.

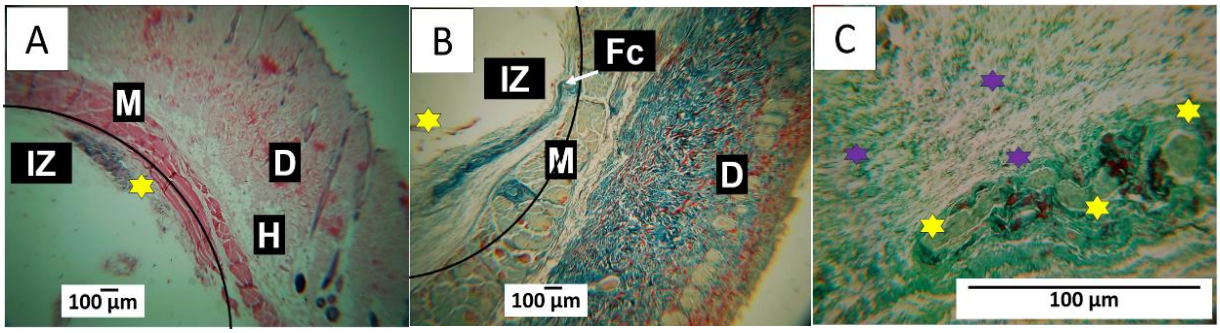

The composite films made of PVA/CS/ZnO-NPs were implanted subdermally, and the results indicate that the degradation process occurred through a foreign body reaction. This was visible through a fibrous capsule surrounding the implantation site and an inflammatory infiltrate with multinuclear cells and giant cells.

When a foreign object is implanted into the body, the immune system interacts with it, and this response can vary depending on the nature of the object and its properties. The process involves a scarring process initiated by the surgical injury caused during the implantation. The exposure of the biomaterial to body fluids like blood and interstitial fluid triggers the healing process.

After implantation, proteins in bodily fluids adhere to the surface of biomaterials. This protein adsorption forms a layer that activates immune system cells such as macrophages and neutrophils. These cells are responsible for defending the body against foreign agents. Upon recognizing the biomaterial as a potential threat, they release cytokines and other inflammatory mediators, which

recruit more immune cells to the site. This determines the initial biological response to the biomaterial [51].

The success of biomaterial integration into the body depends on its compatibility and interaction with tissues and immune cells. Biocompatible materials promoting connective tissue formation are more likely to integrate successfully and form a stable fibrous capsule. However, rejection may occur if the biomaterial elicits a persistent inflammatory response or triggers a robust immune reaction [52].

When it comes to degradable or resorbable materials, the initial process is akin to the one outlined in the preceding paragraph. For certain materials, exposure to bodily fluids abundant in water can trigger hydrolytic degradation, resulting in the fragmentation of the structure. However, in some instances, cells play a crucial role in the enzymatic breakdown of implanted structures, leading to surface erosion and subsequent fragmentation that can be phagocytosed by inflammatory cells. The latter is the mechanism responsible for the degradation/resorption of this study's PVA/CS/ZnO-NPs films.

We began with a film made of PVA 70% and CS 30%, where PVA stabilizes the CS. Figure 8 shows that the material remained stable during the 90-day implantation period, but some fragmentation was observed. Figure 12A (F1) illustrates how inflammatory cells attempted to erode and fragment the material, with the white arrow showing a region where the inflammatory infiltrate penetrated the implantation zone and surrounded fragments of the material. The white oval highlights the accumulation of inflammatory cells. Figure 12B shows the same region at a magnification of 40×, where the accumulation of inflammatory cells can be seen, likely recognizing the material within the foreign body reaction process. Finally, Figure 12C shows formulation F2, where inflammatory cells erode some material particles, leading to further fragmentation.

Figura 12. Fragmentación de películas por actividad celular a 90 días de implantación. A: imagen a 4×, técnica HE. B: Imagen a 40×, técnica HE. C: Imagen a 4×, técnica HE. M: Músculo. II: Infiltrado inflamatorio. Flechas rojas: Células inflamatorias. Estrellas amarillas: Fragmentos del material implantado. Circulo blanco: Acumulo de células inflamatorias. Ovalo blanco: Acumulo celular a una magnificación de 40×. Flechas blancas: indican la zona correspondiente al infiltrado inflamatorio

Figure 12. Fragmentation of films by cellular activity 90 days after implantation. A: image at 4×; HE technique. B: 40× image, HE technique. C: 4× image, HE technique. M: muscle. II: inflammatory infiltrate. Red arrows: inflammatory cells. Yellow stars: fragments of implanted material. White circle: accumulation of inflammatory cells. White oval: Cellular accumulation at 40× magnification. White arrows indicate the area corresponding to the inflammatory infiltrate.

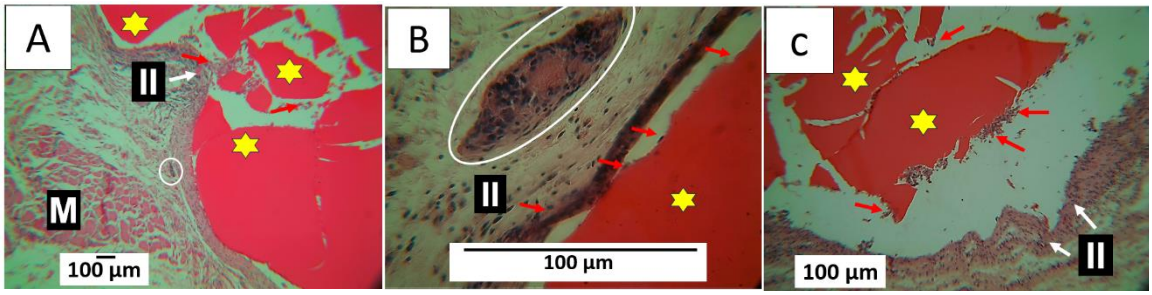

Regenerative therapy necessitates the use of biocompatible, non-cytotoxic, and biodegradable systems with similarities to the target tissue. While the combination of polymers is commonly employed for tissue regeneration, there are inherent disadvantages associated with polymers. This often requires the addition of other components to enhance their physicochemical and mechanical properties. Incorporating nanoparticles can improve these properties by providing a greater loading capacity, which is beneficial for cell proliferation, cell adhesion, and wound healing. Future research should focus on developing Zinc nanoparticles (Zn-NPs) using the drop-casting methodology, as well as exploring the application of these systems in clinical studies for wound treatment.

4. CONCLUSIONS

The FTIR analysis showed the characteristic groups of the PVA/CS mixture, and the addition of the NPs-ZnO did not generate alteration in the spectrum, confirming the homogeneity with the polymer matrix, as shown in F2, F3, and F4. X-ray diffraction analysis confirmed the semicrystalline nature of PVA/CS due to the interactions present between the PVA/CS mixture. The increase in NPs-ZnO content conferred an increase in crystallinity to the polymer matrix, as evidenced in F4. Thermogravimetry analysis demonstrated the thermal stability of the PVA/CS/ZnO composite by increasing the amount of NPs-ZnO and how these play an important role in the stability of the PVA/CS polymer matrix. The study by DSC showed the changes in the maximum temperature values in the endothermic melting peaks and maximum degradation in each of the formulations. SEM morphological analysis showed how the addition of NPs-ZnO produced smooth surfaces in F3 and F4 compared to the porous morphology of PVA/CS, revealing the uniform distribution in the polymer matrix.

The histological studies revealed that all four formulations facilitated continuous tissue healing, as demonstrated by skin and hair recovery. However, during the healing process, a foreign body reaction occurred. F1 was the most stable material among the four formulations, with minimal resorption after 90 days. However, superficial erosion, fragmentation, and partial resorption were

observed. F2 and F3 exhibited an accelerated degradation and reabsorption process due to the inclusion of ZnO-NPs and reduced chitosan, which led to an inflammatory infiltrate responsible for the material degradation process. On the other hand, F4 was almost completely reabsorbed, and connective tissue replacement was observed. The foreign body reaction mechanism mediated by cells facilitated the degradation and resorption process of the PVA/CS/ZnO-NPs films. These findings suggest that ZnO-NP-based scaffolds have significant potential in soft tissue regeneration.

5. REFERENCES

[1] Abdulghani S, Mitchell GR. Biomaterials for in situ tissue regeneration: A review. Biomolecules. 2019;9(11):750.

[2] Krishani M, Shin WY, Suhaimi H, et al. Development of scaffolds from bio-based natural materials for tissue regeneration applications: A review. Gels. 2023;9(2):100.

[3] Biswal T. Biopolymers for tissue engineering applications: A review. Mater Today Proc. 2021;41:397–402.

[4] Feldman D. Poly (vinyl alcohol) recent contributions to engineering and medicine. Journal of composites science. 2020;4(4):175.

[5] Rodríguez-Rodríguez R, Espinosa-Andrews H, Velasquillo-Martínez C, et al. Composite hydrogels based on gelatin, chitosan and polyvinyl alcohol to biomedical applications: A review. International Journal of Polymeric Materials and Polymeric Biomaterials. 2020;69(1):1–20.

[6] Kumar A, Han SS. PVA-based hydrogels for tissue engineering: A review. International journal of polymeric materials and polymeric biomaterials. 2017;66(4):159–182.

[7] Teixeira MA, Amorim MTP, Felgueiras HP. Poly (vinyl alcohol)-based nanofibrous electrospun scaffolds for tissue engineering applications. Polymers (Basel). 2019;12(1):7.

[8] Dattola E, Parrotta EI, Scalise S, et al. Development of 3D PVA scaffolds for cardiac tissue engineering and cell screening applications. RSC Adv. 2019;9(8):4246–4257.

[9] Naghavi Alhosseini S, Moztarzadeh F, Kargozar S, et al. Development of polyvinyl alcohol fibrous biodegradable scaffolds for nerve tissue engineering applications: in vitro study. International Journal of Polymeric Materials and Polymeric Biomaterials. 2015;64(9):474–480.

[10] Vunain E, Mishra AK, Mamba BB. Fundamentals of chitosan for biomedical applications. Chitosan Based Biomaterials Volume 1. Elsevier; 2017. p. 3–30.

[11] Baharlouei P, Rahman A. Chitin and chitosan: prospective biomedical applications in drug delivery, cancer treatment, and wound healing. Mar Drugs. 2022;20(7):460.

[12] Hossain MR, Mallik AK, Rahman MM. Fundamentals of chitosan for biomedical applications. Handbook of Chitin and Chitosan. Elsevier; 2020. p. 199–230.

[13] Islam MM, Shahruzzaman M, Biswas S, et al. Chitosan based bioactive materials in tissue engineering applications-A review. Bioact Mater. 2020;5(1):164–183.

[14] Singh TA, Sharma A, Tejwan N, et al. A state of the art review on the synthesis, antibacterial, antioxidant, antidiabetic and tissue regeneration activities of zinc oxide nanoparticles. Adv Colloid Interface Sci. 2021;295:102495.

[15] Mandal AK, Katuwal S, Tettey F, et al. Current research on zinc oxide nanoparticles: Synthesis, characterization, and biomedical applications. Nanomaterials. 2022;12(17):3066.

[16] Islam F, Shohag S, Uddin MJ, et al. Exploring the journey of zinc oxide nanoparticles (ZnO-NPs) toward biomedical applications. Materials. 2022;15(6):2160.

[17] Gutha Y, Pathak JL, Zhang W, et al. Antibacterial and wound healing properties of chitosan/poly(vinyl alcohol)/zinc oxide beads (CS/PVA/ZnO). Int J Biol Macromol. 2017;103:234–241.

[18] Sirotkin N, Khlyustova A, Titov V, et al. Plasma synthesis and characteristics of nanocomposite coatings based on PVA and chitosan with incorporated nanoparticles for the healing of skin wounds. Mater Chem Phys. 2024;327:129887.

[19] Nathan KG, Genasan K, Kamarul T. Polyvinyl Alcohol-Chitosan Scaffold for Tissue Engineering and Regenerative Medicine Application: A Review. Mar Drugs. 2023.

[20] Castro JI, Valencia-Llano CH, Zapata MEV, et al. Chitosan/polyvinyl alcohol/tea tree essential oil composite films for biomedical applications. Polymers (Basel). 2021;13(21).

[21] Grande-Tovar CD, Castro JI, Tenorio DL, et al. Chitosan–Polyvinyl Alcohol Nanocomposites for Regenerative Therapy. Polymers (Basel) [Internet]. 2023 [cited 2024 May 21];15(23):4595.

[22] Rezaei A, Katoueizadeh E, Zebarjad SM. Investigating of the influence of zinc oxide nanoparticles morphology on the properties of electrospun polyvinyl alcohol/chitosan (PVA/CS) nanofibers. J Drug Deliv Sci Technol. 2023;86.

[23] Coneo N, Ramos Y, De Ávila G, et al. Active chitosan- poly (vinyl alcohol) film reinforced with zinc oxide nanoparticles for food packaging applications. Polymers from Renewable Resources. 2023;14(3).

[24] Rojas K, Canales D, Amigo N, et al. Effective antimicrobial materials based on low-density polyethylene (LDPE) with zinc oxide (ZnO) nanoparticles. Compos B Eng. 2019;172.

[25] AEN/CTN. Evaluación biológica de los productos sanitarios Parte: Parte 6: Ensayos relativos a los efectos locales después de la implantación. 1995.

[26] Du Sert NP, Hurst V, Ahluwalia A, et al. The arrive guidelines 2.0: Updated guidelines for reporting animal research. PLoS Biol. 2020;18(7):1–12.

[27] Kariminejad M, Zibaei R, Kolahdouz-Nasiri A, et al. Chitosan/polyvinyl alcohol/SiO2 nanocomposite films: Physicochemical and structural characterization. Biointerface Res Appl Chem. 2022;12(3):3725–3734.

[28] El-Hefian EA, Nasef MM, Yahaya AH. The preparation and characterization of Chitosan / Poly (Vinyl Alcohol) blended films. E-Journal of Chemistry. 2010;7(4).

[29] Pandele AM, Ionita M, Crica L, et al. Synthesis, characterization, and in vitro studies of graphene oxide/chitosan-polyvinyl alcohol films. Carbohydr Polym. 2014;102(1):813–820.

[30] Yusof YM, Illias HA, Kadir MFZ. Incorporation of NH4Br in PVA-chitosan blend-based polymer electrolyte and its effect on the conductivity and other electrical properties. Ionics (Kiel) [Internet]. 2014 [cited 2024 May 23];20(9):1235–1245.

[31] Gutha Y, Pathak JL, Zhang W, et al. Antibacterial and wound healing properties of chitosan/poly(vinyl alcohol)/zinc oxide beads (CS/PVA/ZnO). Int J Biol Macromol. 2017;103:234–241.

[32] Mansur HS, Sadahira CM, Souza AN, et al. FTIR spectroscopy characterization of poly (vinyl alcohol) hydrogel with different hydrolysis degree and chemically crosslinked with glutaraldehyde. Materials Science and Engineering: C. 2008;28(4):539–548.

[33] Haghighi H, Leugoue SK, Pfeifer F, et al. Development of antimicrobial films based on chitosan-polyvinyl alcohol blend enriched with ethyl lauroyl arginate (LAE) for food packaging applications. Food Hydrocoll. 2020;100:105419.

[34] Tripathi S, Mehrotra GK, Dutta PK. Physicochemical and bioactivity of cross-linked chitosan–PVA film for food packaging applications. Int J Biol Macromol. 2009;45(4):372–376.

[35] Elashmawi IS, Ismail AM, Abdelghany AM. The incorporation of polypyrrole (PPy) in CS/PVA composite films to enhance the structural, optical, and the electrical conductivity. Polymer Bulletin [Internet]. 2023 [cited 2024 May 26];80(10):11379–11399.

[36] Abdelfattah EM, Elzanaty H, Elsharkawy WB, et al. Enhancement of the Structure, Thermal, Linear/Nonlinear Optical Properties, and Antibacterial Activity of Poly (vinyl alcohol)/Chitosan/ZnO Nanocomposites for Eco-Friendly Applications. Polymers (Basel). 2023;15(21).

[37] Jayakumar A, Radoor S, Shin GH, et al. Active and intelligent packaging films based on PVA/Chitosan/Zinc oxide nanoparticles/Sweet purple potato extract as pH sensing and antibacterial wraps. Food Biosci. 2023;56:103432.

[38] Ahmed R, Tariq M, Ali I, et al. Novel electrospun chitosan/polyvinyl alcohol/zinc oxide nanofibrous mats with antibacterial and antioxidant properties for diabetic wound healing. Int J Biol Macromol. 2018;120:385–393.

[39] Saeed A, Guizani I, Hanash FE, et al. Enhancing optical, structural, thermal, electrical properties, and antibacterial activity in chitosan/polyvinyl alcohol blend with ZnO nanorods: polymer nanocomposites for optoelectronics and food/medical packaging applications. Polymer Bulletin 2024 [Internet]. 2024 [cited 2024 May 29];1–26.

[40] Kumar S, Krishnakumar B, Sobral AJFN, et al. Bio-based (chitosan/PVA/ZnO) nanocomposites film: Thermally stable and photoluminescence material for removal of organic dye. Carbohydr Polym. 2019;205:559–564.

[41] Mao D, Li Q, Li D, et al. Fabrication of 3D porous poly (lactic acid)-based composite scaffolds with tunable biodegradation for bone tissue engineering. Mater Des. 2018;142:1–10.

[42] Boccaccini AR, Chen Q, Lefebvre L. Sintering , Crystallisation and Biodegradation Behaviour of Bioglass-Derived Sintering , crystallisation and biodegradation behaviour of Bioglass s -derived glass – ceramics w. 2007;(February). doi: 10.1039/B616539G.

[43] Vicentini DS, Smania A, Laranjeira MCM. Chitosan/poly (vinyl alcohol) films containing ZnO nanoparticles and plasticizers. Materials Science and Engineering: C. 2010;30(4):503–508.

[44] Jayakumar A, Radoor S, Shin GH, et al. Active and intelligent packaging films based on PVA/Chitosan/Zinc oxide nanoparticles/Sweet purple potato extract as pH sensing and antibacterial wraps. Food Biosci. 2023;56:103432.

[45] El-Hefian EA, Nasef MM, Yahaya AH. Preparation and Characterization of Chitosan/Poly(Vinyl Alcohol) Blended Films: Mechanical, Thermal and Surface Investigations. J Chem [Internet]. 2011 [cited 2024 May 29];8(1):91–96.

[46] Anderson JM, Rodriguez A, Chang DT. Foreign body reaction to biomaterials. Semin Immunol. 2008;20:86–100.

[47] Scarritt ME, Londono R, Badylak SF. Host response to implanted materials and devices: An overview. The Immune Response to Implanted Materials and Devices: The Impact of the Immune System on the Success of an Implant. 2016.

[48] Bank RA, Zandstra J, Room H, et al. Biomaterial Encapsulation Is Enhanced in the Early Stages of the Foreign Body Reaction during Conditional Macrophage Depletion in Transgenic Macrophage Fas-Induced Apoptosis Mice. Tissue Eng Part A. 2017;23(19–20):1078–1087.

[49] Balagangadharan K, Dhivya S, Selvamurugan N. Chitosan based nanofibers in bone tissue engineering. Int J Biol Macromol. 2017;104:1372–1382.

[50] Laurenti M, Cauda V. ZnO nanostructures for tissue engineering applications. Nanomaterials. 2017;7(11):374.

[51] Eslami-Kaliji F, Hedayat Nia N, Lakey JRT, et al. Mechanisms of Foreign Body Giant Cell Formation in Response to Implantable Biomaterials. Polymers (Basel). 2023;15(5).

[52] Anderson J, Cramer S. Perspectives on the Inflammatory, Healing, and Foreign Body Responses to Biomaterials and Medical Devices. Host Response to Biomaterials: The Impact of Host Response on Biomaterial Selection. Elsevier Inc.; 2015.